

Prototyping of LAI and FPAR Retrievals From GOES-16 Advanced Baseline Imager Data Using Global Optimizing Algorithm

Yepei Chen, Kaimin Sun , Wenzhuo Li, Chi Chen, Pengfei Li , Ting Bai , Taejin Park, Weile Wang, Ramakrishna R. Nemani , and Ranga B. Myneni

Abstract—The latest Geostationary (GEO) Operational Environmental Satellite-16 (GOES-16) equipped with Advanced Baseline Imager (ABI) has comparable spectral and spatial resolution as low earth orbiting (LEO) sensors [i.e., the Moderate Resolution Imaging Spectroradiometer (MODIS)], but with up-to-the-minute image acquisition capability. This enables greater opportunities to generate two essential climate variables—Leaf area index (LAI) and the fraction of photosynthetically active radiation (FPAR) absorbed by vegetation with more cloud-free observations and at much higher frequency. The improved GEO LAI/FPAR products will increase the capacity for monitoring highly dynamic ecosystems in a timely manner. However, the radiative transfer (RT)-based MODIS operational algorithm cannot be directly applied to GOES-16 ABI data due to different sensor characteristics. Fortunately, it has been shown theoretically and practically, that the RT-based algorithm can be transplanted to any other optical sensors by optimizing the sensor-specific parameters—the single scattering albedo (SSA) and relative stabilized precision (RSP). We built the RT-based ABI-specific lookup tables (LUTs) using a global optimizing algorithm (SCE-UA) that can quickly find the optimal solution. SCE-UA optimizes the SSAs and RSPs in the LUTs by minimizing the difference between ABI and MODIS retrievals and maximizing the main algorithm execution rate. Our efforts indicate that these strategies of parametric optimization is able to decrease the discrepancy between the ABI and MODIS LAI/FPAR products. Comprehensive evaluations were conducted to evaluate ABI retrievals. These indirect inter-comparisons suggest a spatiotemporal consistency between ABI and the benchmark MODIS products, while direct validation with field measurements increases confidence in their accuracy. The proposed approach is applicable to any other optical sensors for LAI/FPAR estimation, especially,

GEO sensors (i.e., Himawari-8, Geo-KOMPSAT-2A, FengYun-4 etc.).

Index Terms—Fraction of photosynthetically active radiation (FPAR), geostationary operational environmental satellite-16 (GOES-16) advanced baseline imager (ABI), global optimizing algorithm (SCE-UA), leaf area index (LAI), moderate resolution imaging spectroradiometer (MODIS).

I. INTRODUCTION

LEAF area index (LAI) [1] and the fraction of photosynthetically active radiation (FPAR) (0.4–0.7 μm) absorbed by vegetation [2], characterizing structure and functioning and energy absorption capacity of vegetation canopy, are two important parameters of many ecological, agronomic, climate, and land surface process models [3]–[5].

In the past decades, several standard LAI/FPAR products have been generated using various types of satellite data, such as the Moderate Resolution Imaging Spectroradiometer (MODIS) LAI/FPAR [6], Visible Infrared Imaging Radiometer Suite (VIIRS) LAI/FPAR [7], LAI/FPAR 3g [8], Global Land Surface Satellites (GLASS) LAI [9], and GEOLAND2 Version 1 (GEOV1) LAI/FPAR [10], etc. These products have been widely used to monitor vegetation phenology, capture impacts of climate change and natural disaster, etc. [5], [11], [12]. However, because of the long revisit time and cloud contamination, all of these products from low earth orbiting (LEO) sensors observations are often so temporally and spatially incomplete that the data usability is greatly reduced [13]. Over the past years, a number of improved geostationary (GEO) satellites have been launched to provide operational earth observations. The newest version of these satellites, such as FengYun-4A [14], Himawari-8 [15], Geostationary Korea Multipurpose Satellite (Geo-KOMPSAT-2A) [16], and Geostationary Operational Environmental Satellite-16 (GOES-16) [17], are equipped with sensors offering images at subhour acquisition interval, while keeping similar spectral and spatial resolutions compared to LEO sensors (i.e., MODIS, VIIRS, etc.). The advantage of hyper-temporal resolution greatly increases the probability of cloud-free observations [18] and expands on the land applications based on LEO sensors [19], [20].

GOES-16 was launched on 19 November 2016 and began operation as GOES-East in December 2017. GOES-16, fixed

Manuscript received February 26, 2021; revised May 22, 2021 and June 28, 2021; accepted July 1, 2021. Date of publication July 7, 2021; date of current version July 22, 2021. This work was supported by the National Natural Science Foundation of China under Grant 41471354, Grant 92038301, Grant 91738301, and Grant 41801344, and in part by the NASA HQ to GeoNEX project exploring geostationary satellite data for land monitoring. (Corresponding author: Kaimin Sun.)

Yepei Chen, Kaimin Sun, Wenzhuo Li, and Ting Bai are with the State Key Laboratory of Information Engineering in Surveying, Mapping and Remote Sensing, Wuhan University, Wuhan 430079, China (e-mail: chenyp@whu.edu.cn; sunkm@whu.edu.cn; alvinlee@whu.edu.cn; baiting@whu.edu.cn).

Chi Chen and Ranga B. Myneni are with the Department of Earth and Environment, Boston University, Boston, MA 02215 USA (e-mail: chenchi@bu.edu; rmyneni@bu.edu).

Pengfei Li is with the School of Computer Science, Hubei University of Technology, Wuhan 430079, China (e-mail: afei200815@gmail.com).

Taejin Park, Weile Wang, and Ramakrishna R. Nemani are with the NASA Ames Research Center, Moffett Field, CA 94035 USA (e-mail: taejin.park@nasa.gov; weile.wang@nasa.gov; rama.nemani@nasa.gov).

Digital Object Identifier 10.1109/JSTARS.2021.3094647

to earth on 75.2° W, high-frequently observes the area over North and South America and the Atlantic Ocean to the west coast of Africa. The Advanced Baseline Imager (ABI) onboard GOES-16 is substantially improved in terms of temporal, spectral, spatial, and radiometric capacity compared to predecessor sensors [21]. ABI has 16 spectral bands with 6 visible/near-infrared (NIR) bands at spatial resolutions of 0.5 km, 1 km, and 2 km and 10 infrared (IR) bands at 2 km [17]. Most of all, ABI obtains a full disk image at the 10-min interval, a CONUS image every 5 min, and images from both mesoscale domains every 60 s. With subhourly image capture intervals, ABI can provide quality-improved LAI/FPAR products with many more cloud-free observations at much higher frequency. This enables greater opportunities to improve the capacity of monitoring highly dynamic ecosystems, including capturing fine-scale phenology [20]. Thus, it is meaningful to retrieve LAI/FPAR from GOES-16 ABI data.

LAI/FPAR products have been operationally produced from MODIS bidirectional reflectance factors (BRFs) since early 2000. Unlike other products like GLASS LAI, LAI/FPAR 3g, and GEOV1 LAI/FPAR, the MODIS product is retrieved by a radiative transfer (RT)-based algorithm without the benchmark LAI/FPARs, while others are based on neural network training. Vegetation clumping is taken into account in the RT-based MODIS algorithm; hence, the MODIS algorithm provides a true LAI, whereas others like the CYCLOPES retrieval algorithm provide an effective LAI [9]. The freely available MODIS LAI/FPAR products derived by MODIS RT-based algorithm have been well tested [22]–[24] and often served as benchmarks to generate and evaluate LAI/FPAR products from other sensor observations [7], [25]–[27]. This demonstrates the high confidence in MODIS RT-based algorithm. However, the MODIS-specific operational algorithm could not be directly applied to other satellite data due to the discrepancies between sensors [7].

Based on the RT theory of canopy spectral invariants, RT-based algorithms can be applied to any optical sensor with the optimization of sensor-specific parameters—the single scattering albedo (SSA) and relative stabilized precision (RSP) [28]. Thus, many efforts have focused on prototyping a MODIS LAI/FPAR algorithm using other satellite data, e.g., AVHRR [28], and VIIRS [7]. Evaluation results show that the quality of retrieved LAI/FPAR products is comparable to that of MODIS products [29], [30]. These studies indicate that with strategies of parametric optimization, the MODIS LAI/FPAR algorithm can be employed to other instruments. To find the optimal parameters for a specific sensor, an exhaustive search method is usually used to try all combinations completely [29], [31]. Thus, the selection of sensor-specific values of parameters is quite computationally intensive and time-consuming. In order to address the problem of parametric optimization, we introduced Shuffled Complex Evolution-University of Arizona (SCE-UA) [32], an efficient and robust model parameter optimization algorithm, to quickly find the optimal sensor-specific parameters.

In this article, we developed an approach to calibrate MODIS operational algorithm for physically deriving ABI LAI/FPARs, which are consistent with MODIS LAI/FPAR products. The SCE-UA algorithm was used to adjust the

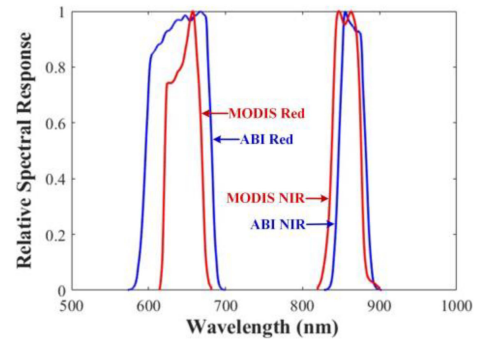


Fig. 1. Comparison of the spectral response for the red and NIR bands between GOES-16 ABI and MODIS.

configurable parameters—SSAs and RSPs by minimizing the difference between ABI and MODIS products and maximizing the main algorithm execution rate. ABI LAI/FPAR products are retrieved based on the newly optimized ABI-specific lookup tables (LUTs). The derived ABI products are compared to similar data sets (e.g., MODIS LAI/FPAR) and validated against field measurements.

The rest of this article is organized as follows. Section II describes the data sets we used in this article. The methodologies for calibrating the LAI/FPAR retrieve algorithm and validating the generated ABI LAI/FPAR are detailed in Section III. Section IV details the comparability of MODIS and ABI SR data and the parameterization specified for ABI. The evaluation results of ABI products are also presented and analyzed in Section IV. Finally, Section VI concludes this article.

II. MATERIALS

A. GOES-16 ABI and MODIS MAIAC BRF

Unlike the LEO sensor MODIS that measures the globe twice a day, the GEO sensor GOES-16 ABI subhourly captures images for about one-third of the earth. MODIS has 36 spectral bands, while ABI provides 16 bands. In this study, only the red and NIR bands are used to retrieve LAI and FPAR products. Fig. 1 depicts the comparison of relative spectral responses at red and NIR bands between the two sensors. Compared with MODIS, ABI has a NIR band with the similar bandwidth and a slight right shift. While for the spectral responses of red band, ABI shows a significant difference from MODIS with a broader bandwidth and a left-shifted center. The discrepancies in spectral responses will lead to a difference in BRDF between the two sensors. Thus, algorithms from MODIS should be adapted and refined when applied for ABI.

Daily GOES-16 ABI BRDF composites and multiangle implementation of atmospheric correction (MAIAC) BRDF products (MCD19A1) were used in this article for comparative analyses. Both products provide sun-sensor geometry and quality information and were collected over the ABI domain in 2018 at a resolution of 0.01° in this article. GOES-16 ABI BRDF data provided by the Geostationary-NASA Earth Exchange (GeoNEX, <https://www.nasa.gov/geonex>), were atmospherically corrected using a customized version of the latest NASA MAIAC

algorithm [33] and geometrically registered to a regular grid in the geographic coordinate system (i.e., latitude/longitude grid). ABI surface BRFs at 15-min interval are daily composited over a three-hour window (9:00–11:00 A.M. for morning composites and 0:00–3:00 P.M. for afternoon composites) by choosing the highest BRF values.

The MCD19A1 Version 6 product is a daily combined MAIAC Land BRF from Terra and Aqua MODIS at a pixel resolution of 500 m [34]. To spatially match the GOES-16 ABI, we reprojected the MODIS MAIAC BRF products to the same grid of ABI data and resampled them to 0.01° resolution.

B. MODIS C6 LAI/FPAR Products

The Terra MODIS 8-day composited LAI/FPAR (MOD15A2H) at 500 m pixel size [35] is used in this article as a benchmark to calibrate MODIS operational algorithm for ABI and evaluate its retrievals. Quality control was conducted to select high-precision and high-quality MODIS LAI/FPARs retrieved from the main algorithm and without contamination. We reprojected the MOD15A2H product from the sinusoidal projection system to latitude/longitude grid as ABI data and resampled them to a pixel size of 0.01° .

C. MODIS Biome Map

The land cover classification is the ancillary data set required by the RT-based MODIS LAI/FPAR algorithm. The latest Collection 6 MODIS Biome Map (MCD12Q1, layer 3,) yearly Terra and Aqua combined at a spatial resolution of 500 m [36] is used in this article. Layer 3 divides the global vegetation land cover into eight types: grasses and cereal crops (B1), shrubs (B2), broadleaf crops (B3), savannahs (B4), evergreen broadleaf forests (B5), deciduous broadleaf forests (B6), evergreen needle-leaf forests (B7), and deciduous needleleaf forests (B8).

To match the spatial grid of GOES-16 ABI, MODIS biome map was reprojected to the geographic coordinate system and resampled to 0.01° resolution by selecting the most occupied biome. Fig. 2 depicts the biome map over ABI domain used in this article. The spatial domain of our study area spans horizontally from 129° W to 33° W, and vertically from 42° N to 48° S. There are almost no deciduous needleleaf forests (B8) over the ABI region. Thus, the calibration of MODIS algorithm and evaluation of retrieved ABI products will not be performed for this biome due to insufficient samples.

D. Evaluation and Validation Sites

Sites from Benchmark Land Multisite Analysis and Inter-comparison of Products (BELMANIP) network were used for site-scale inter-comparison with MODIS benchmarks. These sites are almost flat and homogeneous within a 10×10 km² region. With the high temporal stability, these sites are widely used in the product cross-comparison practice [29].

Land Products (LPs) (unscaled LAI/FPAR ground-based reference maps at $300 \text{ m} \times 300 \text{ m}$ pixel size) from Ground-Based Observations for Validation (GBOV¹) were used in this article

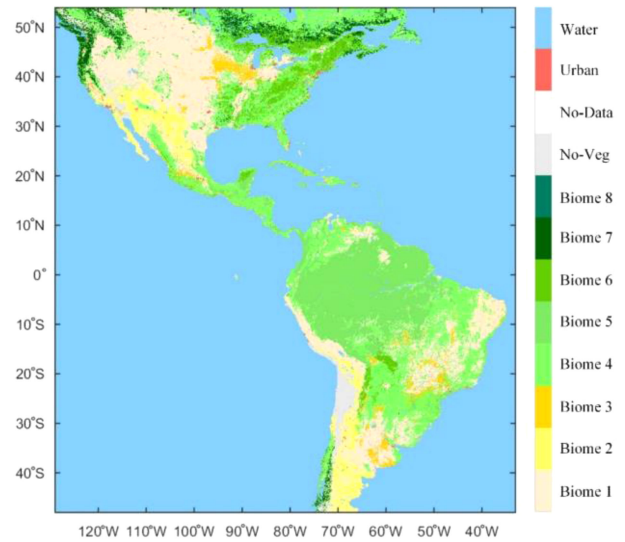


Fig. 2. Biome map over ABI domain used in this article.

to validate the ABI retrievals [37]. In addition to the LP values themselves, per-pixel quality indicators are provided to identify pixels.

III. METHODS

A. Analysis of GOES-16 ABI and MODIS MAIAC BRF

We investigated the difference between GOES-16 ABI and MODIS MAIAC BRF by matching GOES-16 ABI and MODIS MAIAC BRF pairs through quality control and sun-sensor geometry control. To achieve a reliable analysis of BRF discrepancies, only observations with high quality were used. These images were cloud, shadow, and snow free, and with low aerosols. We minimized the difference in sun-sensor geometry between GOES-16 ABI and MODIS by only including observation matchups meeting with the following criteria.

- 1) The difference of solar zenith angle is less than 15° .
- 2) The difference of sensor zenith angle is lower than 15° .
- 3) The difference of relative azimuth angle between the two sensors' observations is smaller than 30° .

B. Calibration of MODIS LAI/FPAR Algorithm

The MODIS operational algorithm derives LAI/FPAR with red and NIR-band BRFs, their uncertainties, sun-sensor geometry, and biome map as inputs [38]. It consists of a three-dimensional (3-D) RT-based main procedure, and the backup algorithm based on empirical relationships between normalized difference vegetation index and LAI/FPAR. If the main algorithm failed, the back-up algorithm was activated to estimate LAI/FPAR. The evaluation of the MODIS LAI/FPAR algorithm enhances the basis for the usage of the algorithm [39], [40].

The BRF of canopy can be separated into two components: the radiometric contribution from single scattering and the structural contribution from multiple scattering. The probability of a single scattering event (SSA) depends on the wavelength, while the recollision probability is wavelength independent and

¹[Online]. Available: <https://gbov.acri.fr/>

completely determined by the canopy structure. The “spectral invariants theory” or “p-theory” describes the unique positive eigenvalue of the RT equation as the product of the SSA and a wavelength-independent parameter (p) [7], [41], [42]. According to the spectral invariant principle, it is possible to reconstruct the radiation field of the canopy at any wavelength if knowing the invariants of the canopy and the SSA of an average phytoelement at any wavelength [43]. This theory lays the foundation of optimizing sensor-specific parameters to achieve consistency of LAI/FPAR retrievals between different sensors. The MODIS operational algorithm retrieves LAI/FPAR by generating a LUT through 3-D RT equation. The LUT stores modeled BRFs as a function of SSA, for diverse LAIs and sun-sensor geometries. The LAI/FPAR solutions are located by comparing the simulated BRFs and those observed from the satellite. The wavelength-dependent parameter SSA is also varying with sensor spatial resolution [30]. A BRF can be computed for the sensor-specific spectral bands and spatial resolution by tuning the SSA [42]. Therefore, the SSA is our first adjustable parameter when transplanting the MODIS operational algorithm to other optical sensors.

In general, only the surface reflectance cannot provide sufficient information to estimate a unique LAI value, which is treated as “ill-posed” problem. Therefore, a particular surface reflectance is corresponding to a set of LAI/FPARs, considered as acceptable solutions [7]. The main procedure of MODIS operational algorithm is formulated as follows: All candidates of LAI and FPAR for which the difference between observed ($r = (r_1, r_2, \dots, r_N)$) and modeled ($r_M = (r_{M,1}, r_{M,2}, \dots, r_{M,N})$) entries stored in the LUT at N spectral bands is equal to or smaller than the corresponding uncertainty, i.e.,

$$\chi_\delta^2[r - r_M] = \sum_{k=1}^N \left(\frac{r_k - r_{M,k}}{\delta k} \right)^2 \leq N \quad (1)$$

are taken as acceptable solutions. Here δ is a stabilized precision introduced by Wang *et al.* as a function ($\delta^2 = (\sigma^2 + \sigma_M^2)/\theta^2$, here θ is a stabilization parameter determined by σ and σ_M) of observation uncertainty σ and model uncertainty σ_M [44]. Assuming the deviations, $\varepsilon_k = (r_k - r_{M,k})/\sigma_k$, $k = 1, 2, \dots, N$ follows a Gaussian distribution. The random variable $\chi_\delta^2[r - r_M]$ has a chi-square distribution. The LAI/FPARs satisfy the inequality $\chi_\delta^2 \leq N$ indicate good precision. The averaged LAI/FPAR and their dispersions calculated from the acceptable solutions are reported as retrievals and their uncertainties [38].

Let $m = (m_1, m_2, \dots, m_N)$ and $m_M = (m_{M,1}, m_{M,2}, \dots, m_{M,N})$ represent the true BRFs and model predicted expected values. Based on the Minkowski inequality, the $\chi_\delta[r - m]$ can be transformed as follows:

$$\chi_\delta[r - r_M] \leq \chi_\delta[r - m] + \chi_\delta[r_M - m_M] + \chi_\delta[m - m_M]. \quad (2)$$

The inequality shows that χ_δ depends on how the modeled BRF differs from both the observed and true BRF. Therefore, the calibration is simplified to searching the SR model that optimally approximates both the true and observed BRFs [31]. It is obvious the observation and model uncertainties matter to solve this

problem. Input data and their uncertainties are, “in general, the minimal information necessary to construct approximate solution for ill-posed problems” [45]. The RSP (δ), which actually takes into account both the remote sensing observations and the model uncertainty, is therefore the second optimized parameter for calibrating MODIS operational algorithm.

C. ABI-Specific LUT Optimization Using SCE-UA

The theory of spectral invariants allows transplanting the MODIS operational algorithm to ABI by optimizing the sensor-specific parameters of SSAs and RSPs. Since uncertainties in the NIR reflectance are minimally influenced by the differences in spectral bandwidth and data resolution [30], MODIS RSPs at NIR band for each biome are inherited by ABI and remain constant in the tuning procedure. Therefore, the key to transplanting the MODIS operational algorithm is to search the three parameters (SSAs at red and NIR bands and RSPs at red band) specific for ABI sensor characteristics. It is impossible to measure the SSA and RSP at pixel scale; thus, the well-validated MODIS products with high confidence serve as the benchmarks to locate the optimal ABI SSAs and RSP combination.

The selection of the optimal ABI SSAs and RSP combination is according to the performance metrics, including:

- 1) the retrieval index (RI);
- 2) the root mean squared error (RMSE) between ABI and MODIS LAIs; and
- 3) the proximity of ABI and MODIS LAI histograms [7], [31].

The RI is the proportion of the pixels retrieved by the main algorithm, defined as

$$RI = \frac{\text{number of pixels retrieved from the main algorithm}}{\text{number of total processed pixels}}. \quad (3)$$

While the RI describes the spatial coverage of the retrievals with high quality and precision, the RMSE indicates accuracy, characterizing the difference between ABI and the benchmark MODIS retrievals, that is

$$RMSE = \sqrt{\frac{1}{N} \sum_{i=1}^N (LAI_{ABI}(\omega, \delta, i) - LAI_{MODIS}(i))^2}. \quad (4)$$

The calibration procedure is to find an optimal combination of red- and NIR-band SSAs (ω_{red} , and ω_{NIR}) and RSP at red band (δ_{red}) that: 1) maximizes the RI and 2) minimizes the RMSE and the disagreement between the histograms. In previous studies [7] and [31], to find the optimal values of SSA and RSP; the RI and RMSE were calculated for every valid combination. It is computationally intensive to try all combinations within a valid range at a small step completely. Thus, we introduce SCE-UA, a global optimization algorithm used in model calibration, to find the proper combination quickly with much less iterations.

SCE-UA has been successfully employed in extensive studies to solve optimization problems [46], [47]. It employs a clustering strategy to focus the search towards regions that tend to be more favorable, which greatly improves the search efficiency and the ability to find the global optimal parameters [48]. The

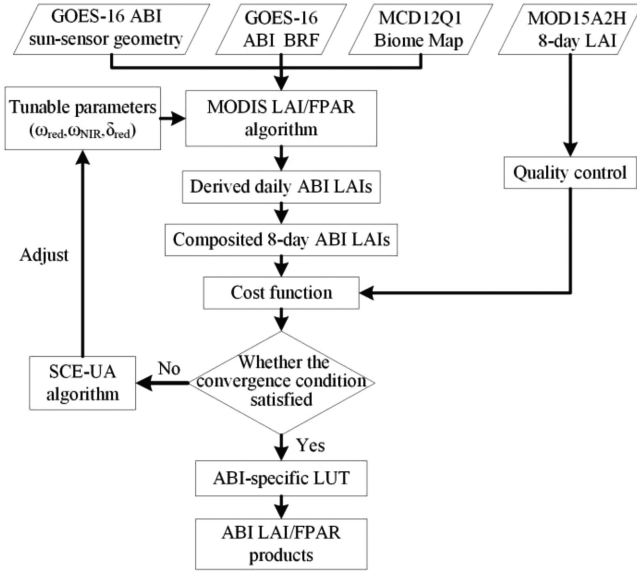


Fig. 3. Flow chart of calibrating MODIS operational LAI/FPAR algorithm by using SCE-UA algorithm to build optimized ABI-specific LUT.

algorithm is not sensitive to the initial values of the configurable parameters [48]. With these advantages, SCE-UA was adopted to calibrate MODIS LAI/FPAR algorithm to achieve inter-sensor consistency. The cost function used in this article is defined as

$$y = \frac{1}{RI} + RMSE. \quad (5)$$

MODIS-specific SSAs and RSP are taken as the initial values of the configurable parameters, thus, SCE-UA will converge to the optimal solution much earlier. The optimization is successful only when the coefficient of variation of the continuous five minimum cost function is smaller than 0.001. The SSAs in the red (ω_{red}) and NIR (ω_{NIR}) bands and RSP at red band (δ_{red}) corresponding to the minimum value of cost function are the optimal solution.

MODIS operational algorithm calibration is carried out by searching for a set of parameters (ω_{red} , ω_{NIR} , and δ_{red}) that optimize the values of metrics (RI and RMSE) that quantify the performance of the algorithm using ABI data (as shown in Fig. 3). First, ABI daily LAI were derived with MODIS-specific SSAs and RSPs as initial values for configurable parameters, and then composited daily LAI to 8-day frequency. Second, we calculated the RI and RMSE between ABI LAI and MODIS LAI. If the value of cost function is small enough (maximum RI and minimum RMSE) to meet the convergence condition, then the optimal SSAs and RSP are obtained. If the opposite happens, the SCE-UA optimization algorithm will be performed to search a set of more favorable parameters within a defined range at a defined step to generate new ABI LAI products. We perform the loop iteration, until reaching the termination condition. Third, the top 10 sets of parameters sorted by ascending objective function value from SCE-UA were separated. Finally, we selected the set (ω_{red} , ω_{NIR} , and δ_{red}) which minimized the disagreement of the LAI histograms as the optimal solution for

ABI. Only the pixels with high quality as retrieved from main algorithm and not contaminated were used in the optimizing procedure. It should be noted that the configurable parameters in MODIS LUT is biome specific and we conducted optimizing procedure biome by biome. ABI LAI/FPAR profiles will be derived used the ABI-specific LUT obtained by SCE-UA, and comprehensively evaluated with similar data set and available ground measurements.

D. Evaluation of Derived ABI LAI/FPAR Products

To assess the derived ABI LAI/FPAR, we complemented both direct validation with ground truth data and indirect inter-comparisons with similar data sets. In this article, MODIS LAI/FPAR products served as benchmarks to evaluate ABI LAI/FPAR at full disk and site scale, respectively. In case of global evaluation, we compared the aggregated ABI LAI/FPAR products with reference data at 8-day and seasonal scales, respectively. Sites from BELMANIP2.1 network were selected for further inter-comparison between the ABI and MODIS products at the site scale. We matched the valid LAI/FPAR pairs from ABI and MODIS over a $3 \text{ km} \times 3 \text{ km}$ area for each BELMANIP 2.1 sites, which allows limiting the effects of point spread function and geometric accuracy [10]. The overall spatiotemporal consistency between the ABI and MODIS retrievals was evaluated by biome type. A set of statistical metrics [Bias, RMSE, and coefficient of determination (R^2)] were utilized to indicate the discrepancy between the MODIS and ABI retrievals. It should be noted that for both ABI and MODIS products only retrievals with high quality and derived from the main algorithm were used in the evaluation procedure.

Due to the resolution-mismatch, geolocation errors, the fine-resolution reference maps up-scaled from in situ measurements are recommended to validate coarse resolution remote sensing products instead of directly using ground data [49], [50]. Since the widely used DIRECT 2.0 ground database (2000–2017) has no field measurements available during the GOES-16 ABI era (2018–present), the accuracy assessment of ABI products was performed using the field-measurements-derived reference maps from GBOV collected in 2018. The uncertainty is measured by using the RMSE between retrievals and reference maps. Note that the spatial coverage used is $3 \text{ km} \times 3 \text{ km}$ (i.e., average values of 3×3 pixels in case of ABI products, and 10×10 pixels for GBOV). In case of GBOV, the ancillary quality indicator providing the number of the valid observations at the primary high resolution (20 m) was used, and 300 m-resolution pixels with less than 70% of valid primary data were masked out. To ensure the land cover homogeneity, the information entropy proposed by [23] was adopted in this article. We selected the GBOV sites that the information entropy is smaller than 1 [29] and the fraction of the majority land cover type (excluded water body and urban area) is no less than 60% over a $3 \text{ km} \times 3 \text{ km}$ area. In order to achieve the accurate assessment, the closest ABI retrievals date to the ground measurements were used. The mean values of quality-controlled ABI products via main algorithm over the $3 \text{ km} \times 3 \text{ km}$ area that contained more than 60%

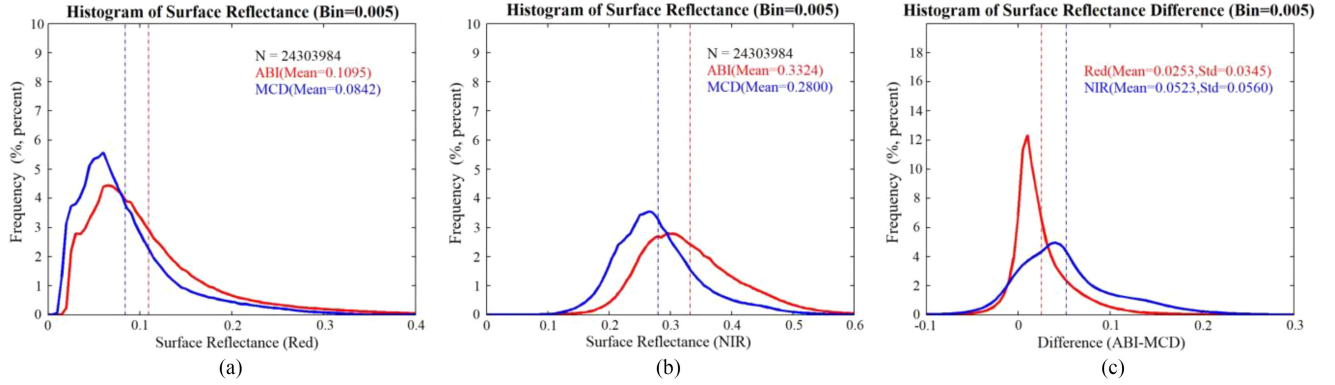


Fig. 4. Comparison of BRF from ABI and MCD products at the red and NIR bands across all biomes over the ABI domain during the winter (January 1–31) and summer (July 1–31) of year 2018. (a) Histogram of BRF at the red band across all biome for ABI and MCD, respectively. (b) Histogram of BRF at the NIR band across all biome for ABI and MCD, respectively. (c) Histogram of absolute BRF difference (ABI-MCD) at the red and NIR bands across all biomes.

TABLE I
BIOME-SPECIFIC MEAN AND STANDARD DEVIATION OF SURFACE REFLECTANCE DIFFERENCES BETWEEN ABI AND MCD AT RED AND NIR BANDS AT SEASONAL SCALE IN 2018

Biome Type	January			July		
	N	Red	NIR	N	Red	NIR
B1	5336277	0.045±0.050	0.060±0.062	10567840	0.028±0.036	0.050±0.054
B2	2764297	0.055±0.053	0.054±0.052	1514754	0.060±0.063	0.053±0.053
B3	679771	0.034±0.042	0.054±0.061	1010111	0.037±0.039	0.072±0.068
B4	3579202	0.031±0.031	0.063±0.058	7774335	0.019±0.022	0.051±0.057
B5	638936	0.016±0.016	0.049±0.055	2328010	0.012±0.114	0.062±0.055
B6	486715	0.044±0.032	0.095±0.060	875186	0.013±0.013	0.046±0.053
B7	118834	0.022±0.026	0.058±0.072	233399	0.012±0.016	0.020±0.055

valid retrievals were calculated to compare with ground-based reference data.

IV. RESULTS

A. Surface Reflectance Difference

We used all available daily ABI and Terra and Aqua combined MODIS (MCD) observations over the ABI domain in January and July in 2018 with the best quality and minimal difference in sun-sensor geometry to quantify the BRF difference. Fig. 4 shows the histograms of BRFs for all biomes at red and NIR bands from ABI and MODIS, as well as the BRF difference between them. ABI shows higher red-band BRF [see in Fig. 4(a)] and NIR-band BRF [see in Fig. 4(b)] than MODIS. This is probably due to wider red band and its shift to shorter wavelength range. The shift of NIR band to a longer wavelength range is a reason why we see higher NIR [17]. From Fig. 4(c), we can see that the BRF difference at NIR band (mean difference is 0.0523) is much higher than that at red band (mean difference is 0.0253). There are obvious BRF shifts from MODIS to ABI at the two bands and discrete distribution of BRF difference between MODIS and ABI at NIR band. This indicates that it is necessary to do the optimization of the sensor-specific parameters. Therefore, the primary objective of

this article is to calibrate MODIS algorithm to build ABI-specific LUT to address the discrepancy between the MODIS and ABI sensor.

Table I summarizes the mean and standard deviation of red- and NIR-band BRFs difference per biome at seasonal scale. Discrepancies of BRF between ABI and MCD in January and July demonstrate the same pattern: ABI BRF is higher than MODIS BRF at both red and NIR band. Hence, instead of inheriting from MODIS LUT, the RSP need to be adjusted for ABI-specific BRFs uncertainty. The three non-forest biome types (B1-B3) shows much higher standard deviation of BRFs difference than other biomes in red band. It is possible that the RSP difference between ABI and MODIS parametric configurations in red band for the three biomes will be larger than that for other biomes.

B. ABI-Specific Parameterization

We used the daily 3h composited (around 10:30 A.M.) ABI SR data over ABI domain during winter (January 1–8) and summer (July 4–11), which are spatially and temporally representative enough and sufficient in number, to solve the parametric optimization problem. The optimal parameters, with the maximal RI and minimal RMSE compared to MODIS products, were finally

TABLE II
BIOME- AND SPECTRAL-SPECIFIC SSAs AND RSPs USED IN THE MODIS OPERATIONAL ALGORITHM AND ADJUSTED FOR THE ABI DATA. THE DIFFERENCES OF SSAs AND RSPs BETWEEN ABI AND MODIS PARAMETRIC CONFIGURATIONS ARE ALSO LISTED IN THE TABLE

		B1	B2	B3	B4	B5	B6	B7
ABI	ω_{red}	0.225	0.222	0.151	0.177	0.103	0.209	0.240
	ω_{NIR}	0.897	0.861	0.951	0.903	0.989	0.903	0.773
	δ_{red}	0.22	0.28	0.29	0.20	0.29	0.29	0.30
MODIS	ω_{red}	0.180	0.160	0.100	0.140	0.151	0.140	0.140
	ω_{NIR}	0.880	0.840	0.940	0.880	0.910	0.840	0.700
	δ_{red}	0.20	0.20	0.20	0.20	0.30	0.30	0.30
ABI-MODIS	$\Delta\omega_{\text{red}}$	+0.045	+0.062	+0.051	+0.037	-0.047	+0.069	+0.100
	$\Delta\omega_{\text{NIR}}$	+0.017	+0.021	+0.011	+0.023	+0.079	+0.063	+0.073
	$\Delta\delta_{\text{red}}$	+0.02	+0.08	+0.09	0.00	-0.01	-0.01	0.00

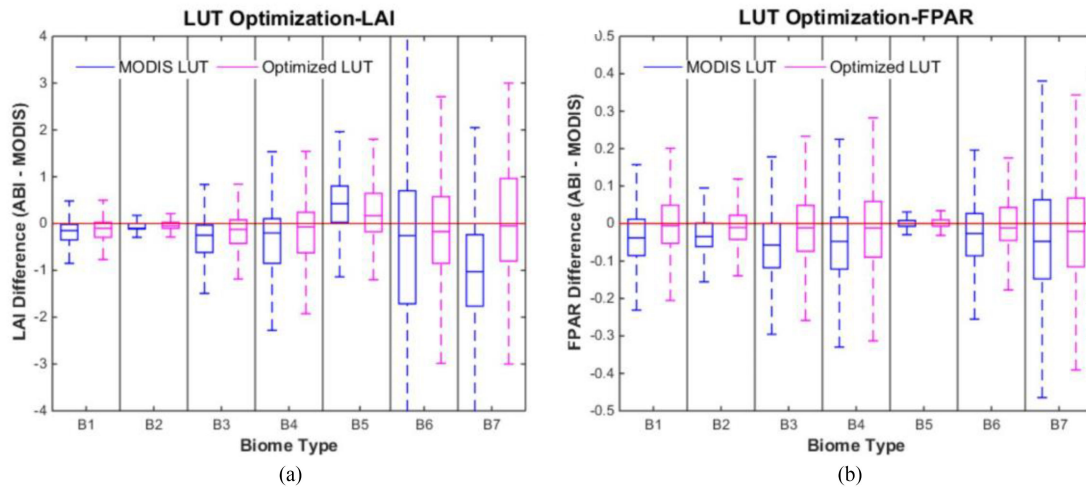


Fig. 5. Distributions of LAI/FPAR difference (ABI-MOD) before (using MODIS LUT) and after optimization. (a) LAI. (b) FPAR. LAI/FPAR retrievals over ABI domain during a compositing period (July 12–19) in 2018 are used in this analysis. The blue and magenta boxplots depict the distributions of LAI/FPAR difference using the MODIS LUT and the newly optimized ABI LUT, respectively. The central magenta line in each box plot stands for the median value of differences.

located through adjustment using SCE-UA. Table II details the values of the biome- and spectral-specific SSAs and RSPs in MODIS LUT and newly optimized ABI-specific LUT. The SSAs and RSPs differences between MODIS and ABI configurations are also listed in Table II. ABI shows larger NIR-band SSAs for all biomes, while larger red-band SSAs are observed in case of most biomes, except for B5. The SSA changes are mostly consistent with the BRFs shifts analyzed in Section III-A. The difference of RSP between ABI and MODIS configurations at the red band is larger for B1, B2, and B3 than other biomes. This is probably due to that, the uncertainty of ABI BRFs at the red band differs from that of MODIS red-band BRFs in case of B1, B2, and B3.

To understand the improvement on retrievals after sensor-specific parameter adjustment, we apply the operational MODIS LUT and newly optimized ABI LUT to the ABI SR respectively. The retrievals before and after optimization were compared in terms of difference to MODIS products and the main algorithm execution rate. Fig. 5 shows the biome-specific distributions of LAI/FPAR differences between ABI and MODIS before and after parametric adjustment. ABI SR and its LAI/FPAR retrievals over ABI domain during July 12–19 in 2018 were used in this analysis, as well as the corresponding reference

MODIS LAI/FPAR products. The forest biomes (B5–B7) show a higher LAI difference, whereas nonforest biomes (B1–B4) exhibit relatively larger FPAR disparity. The forest biomes also present larger uncertainties than nonforest biomes when it comes to LAI. Direct application of MODIS LUT to ABI data without any parametric adjustment, resulted in underestimation of LAI and FPAR for most biomes except for B5. After sensor-specific parameter optimization, the differences of both LAI and FPAR between MODIS and ABI are clearly reduced. The median value of LAI differences are dropped from -0.15 to -0.1 for B1, from 0.43 to 0.17 for B5, and from -0.26 to -0.17 for B6. In case of FPAR, the obvious decreases of median difference are observed for B1 (from -0.038 to -0.006), B3 (from -0.057 to -0.012), and B4 (from -0.048 to -0.012). For both LAI and FPAR, the ranges of difference between ABI and MODIS are smaller after optimization for each biome. These results indicate that the sensor-specifically parameter optimization is necessary and it enables ABI retrievals comparable with the reference MODIS products.

The proposed adjustment procedures can also improve the main algorithm execution rate. The stacked bars in Fig. 6 presents the biome-specific comparison of algorithm retrieval rates before (MODIS LUT) and after (newly optimized ABI

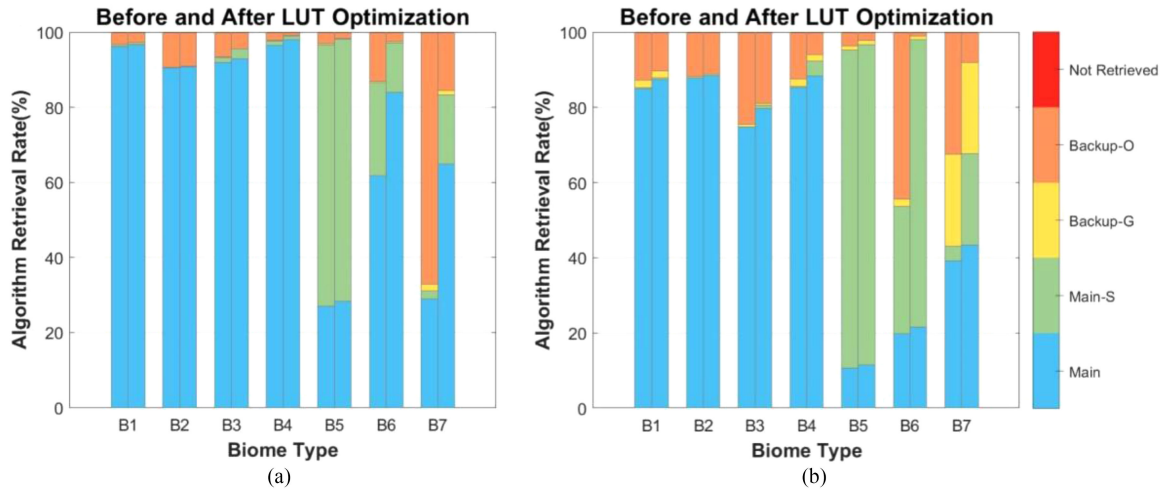


Fig. 6. Algorithm retrieval rate (%) of ABI before (using MODIS LUT) (left bars) and after optimization (right bars) for different biome types at the full disk scale during the (a) boreal winter (January 9–17) and (b) summer (July 12–19) of year 2018. The five types of algorithm paths (from highest to lowest quality) are flagged as: the main algorithm without saturation (Main), the main algorithm with saturation (Main-S), the backup algorithm due to sun-sensor geometry (Backup-G), and the backup algorithm due to other reasons (Backup-O).

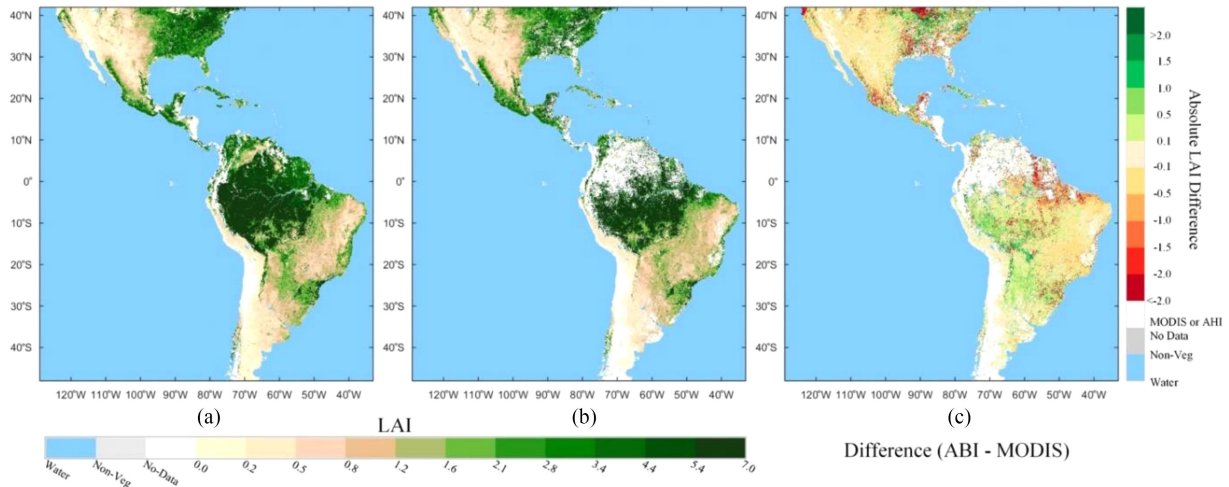


Fig. 7. Comparison of spatial distributions of LAI from ABI and MODIS products over the ABI domain during the summer (July 12–19) of year 2018. (a) ABI LAI. (b) MODIS LAI. (c) LAI difference between ABI and MODIS. No-data pixels in white color are observations contaminated by cloud, cloud shadow, aerosol, etc. The missing data rate of ABI LAI is much lower than that of MODIS LAI benefiting from observations that are more frequent.

LUT) parametric optimization at the full disk scale. Fig. 6(a) and (b) shows the results in the winter (January 9–17 in 2018), and summer (July 12–19 in 2018) respectively. The RI (the execution rate of Main and Main-S algorithm) is one of key indicators, representing the quality of retrievals. From Fig. 6, we can see that the RIs are increased after LUT optimization for all biomes, especially for forest biomes (B6 and B7), in both winter [see Fig. 6(a)] and summer [see Fig. 6(b)] seasons. The RI for B6 increases from 86.53% to 97.17% in winter and from 53.66% to 97.97% in summer. In case of B7, the RI climbs from 31.06% to 83.28% and from 43.07% to 67.67%, respectively, in winter and summer.

C. Intercomparison With MODIS LAI/FPAR

After the sensor-specific parameter optimization, we generated ABI LAI/FPARs over the ABI domain in 2018 using the

newly optimized ABI LUT. To assess the performance of the proposed strategy of parametric optimization and the reliability of the ABI retrievals, the derived ABI LAI/FPARs were further spatiotemporally evaluated, with MODIS products as benchmarks, at full disk scale and site scale, respectively.

1) *Full Disk Scale*: Fig. 7 depicts the spatial distributions of ABI and MODIS LAI, respectively, over the ABI domain during the summer (July 12–19) of 2018, as well as the difference between them. Fig. 8 presents the same but for FPAR patterns. From Figs. 7 and 8, ABILAI/FPAR maps show much fewer gaps (characterized as no-data pixels colored in white) than MODIS LAI/FPAR maps. In case of ABI LAI/FPAR, the missing data rate is 10.10%, but it is up to 25.08% when it comes to MODIS LAI/FPAR. These figures suggest that ABI can provide much more cloud-free observations, which benefits from the up-to-minute image acquisition frequency. The advantage of spatially

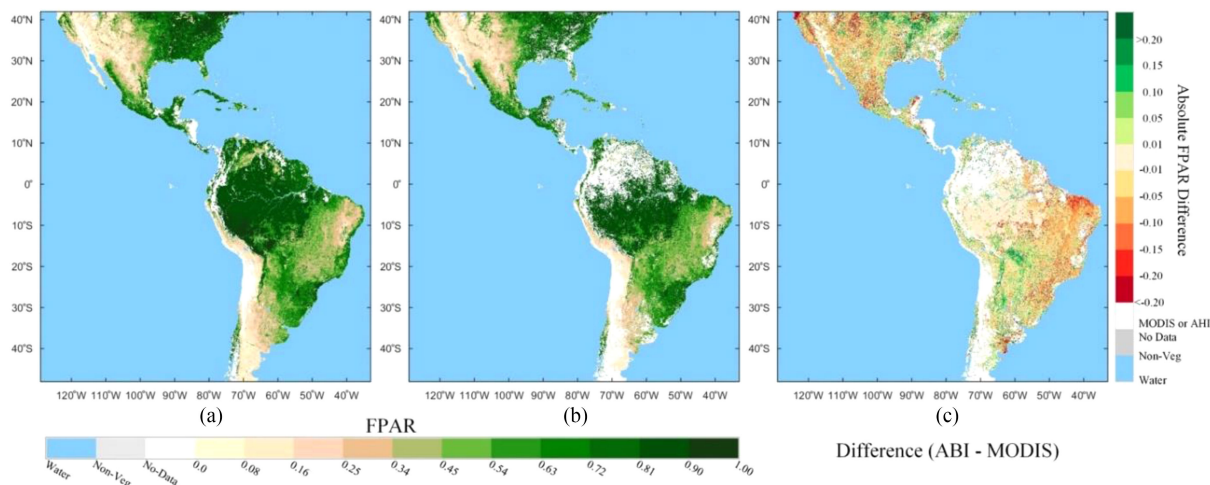


Fig. 8. Comparison of spatial distributions of FPAR from ABI and MODIS products over the whole ABI domain during the summer (July 12–19) of year 2018. (a) ABI FPAR. (b) MODIS FPAR. (c) FPAR difference between ABI and MODIS. No-data pixels in white color are observations contaminated by cloud, cloud shadow, aerosol, etc. The missing data rate of ABI FPAR is much lower than that of MODIS FPAR benefiting from more frequent observations.

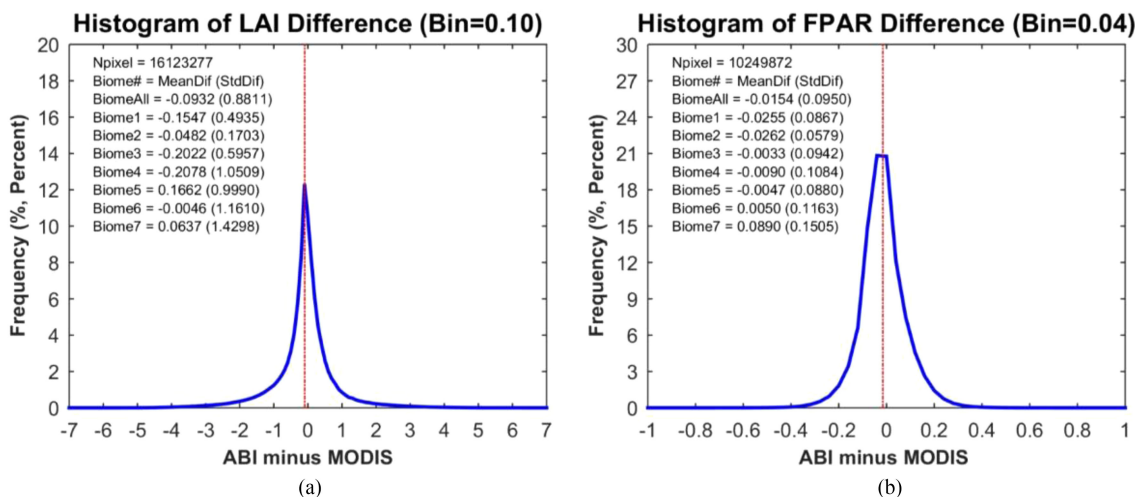


Fig. 9. Histogram depicting LAI/FPAR comparison between ABI and MODIS over the AB domain during the summer (July 12–19) of year 2018. (a) LAI. (b) FPAR.

and temporally continued ABI products will greatly contribute to capturing disaster impacts, vegetation phenology, etc.

In Figs. 7(a), (b) and 8(a), (b), we can see that LAI and FPAR from ABI and MODIS show similar spatial distribution patterns. Forests show high LAI/FPAR values while low values are observed over nonforest regions. Tropical forests, i.e., Amazon rain forests, show high LAI/FPAR values (colored in dark green), while grasslands, and shrub lands, i.e., Western America and Southern Argentina, fall low LAI/FPAR domain.

The spatial distribution of ABI LAI shows a good agreement with that of MODIS LAI, when comparing Fig. 7(a) and (b). The LAI differences between ABI and MODIS are shown in Fig. 7(c). The overall discrepancies of LAI are mostly within a small range (mostly within ± 0.5), while larger differences appear over the dense forest. No systematic bias between ABI LAI and MODIS LAI is observed in difference map. The same patterns for FPAR can be observed in Fig. 8. The ABI FPAR [see Fig. 8(a)] spatially coincides well with MODIS FPAR

[see Fig. 8(b)], as the differences [see Fig. 8(c)] between them are mostly within ± 0.10 . As shown in Fig. 5, underestimation tendency of LAI/FPAR can be found in B1, B3, and B4 (Biome map is shown in Fig. 2). Larger LAI differences are located at high LAI levels, while smaller differences appear in relatively low LAI domains. This is partially because of the reflectance saturation in dense vegetation canopies [29]. The spatial distributions and difference maps of LAI/FPAR demonstrate spatial consistency of LAI/FPAR between ABI and MODIS.

To detail the differences of LAI/FPAR between ABI and MODIS, further analysis of histograms of the differences are depicted in Fig. 9. This figure also provides the biome-specific means and standard deviations. The LAI [see Fig. 9(a)] and FPAR [see Fig. 9(b)] differences distribute quite symmetrically about mean values. Consistency of LAI and FPAR between ABI and MODIS can be observed, as more than 80% of LAI differences are within ± 0.25 , and more than 80% of FPAR differences are between ± 0.05 . These figures indicate that the ABI

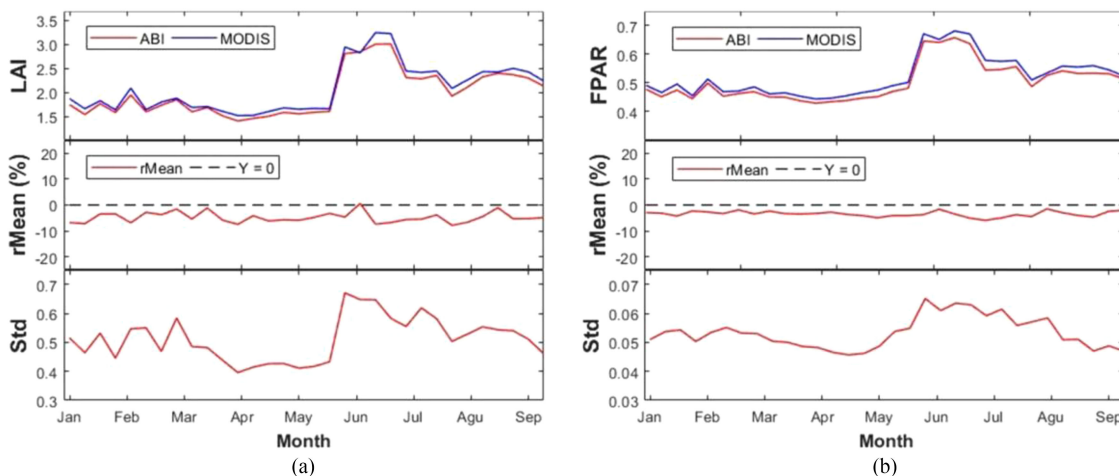


Fig. 10. Temporal comparison between ABI LAI/FPAR and MODIS LAI/FPAR over the ABI domain. Global mean LAI/FPAR from ABI and MODIS at an 8-day interval during January to September in 2018 are shown here. The top panel shows seasonal variation of ABI and MODIS LAI/FPAR retrievals, while the bottom two panels show the relative mean (rMean) and standard deviation (Std) of difference between them. (a) LAI. (b) FPAR.

LAI/FPAR retrievals agree with MODIS reference data, with an overall mean difference of -0.0932 for LAI and -0.0154 for FPAR.

Fig. 10 shows the seasonality of ABI and MODIS 8-day composited LAI/FPAR from January to September in 2018. Fig. 10(a) and (b) depicts the 8-day LAI and FPAR time series from ABI and MODIS, respectively, as well as the relative mean and standard deviation of the difference between them. The difference between ABI and MODIS was calculated for each pixel first, and then the mean was aggregate for all pixels. The ABI time series show similar seasonality with those from MODIS. In the cases of both LAI and FPAR, a peak in summer can be observed because of the vegetation growing season in northern hemisphere. As expected, higher LAI/FPAR values (up to 3.2 for LAI and 0.66 for FPAR) are observed during the boreal summer (e.g., July), while much lower LAI/FPAR values (about 1.5 for LAI and 0.43 for FPAR) appear in boreal winter (e.g., January). This can be explained by the fact that the dominant vegetation (e.g., B1, B6, and B7) in northern hemisphere shows strong seasonal LAI/FPAR variations, reaching their peaks in summer and drop to bottom in winter. The Amazon evergreen broadleaf forests (B5) and shrub lands (B2) dominating in the southern hemisphere show weak LAI/FPAR seasonality, remaining stable throughout the year (see in Fig. 2 of biome map over ABI domain). The standard deviation of differences between ABI and MODIS retrievals have similar seasonal behavior, as larger values (up to 0.67 for LAI and 0.065 for FPAR) appear in boreal summer and smaller values (about 0.40 for LAI and 0.045 for FPAR) are observed in boreal winter. The standard deviation of differences are closely related to the LAI/FPAR magnitudes, possibly due to the large variations caused by saturation in dense forests [29]. The results demonstrate a good temporal consistency between ABI LAI/FPAR retrievals and MODIS products.

2) *Site Scale*: For comprehensive evaluation of the ABI retrievals, we conducted an overall spatiotemporal comparison to MODIS products over all available BELMANIP-2.1 sites. ABI LAI/FPAR retrievals and corresponding MODIS products at

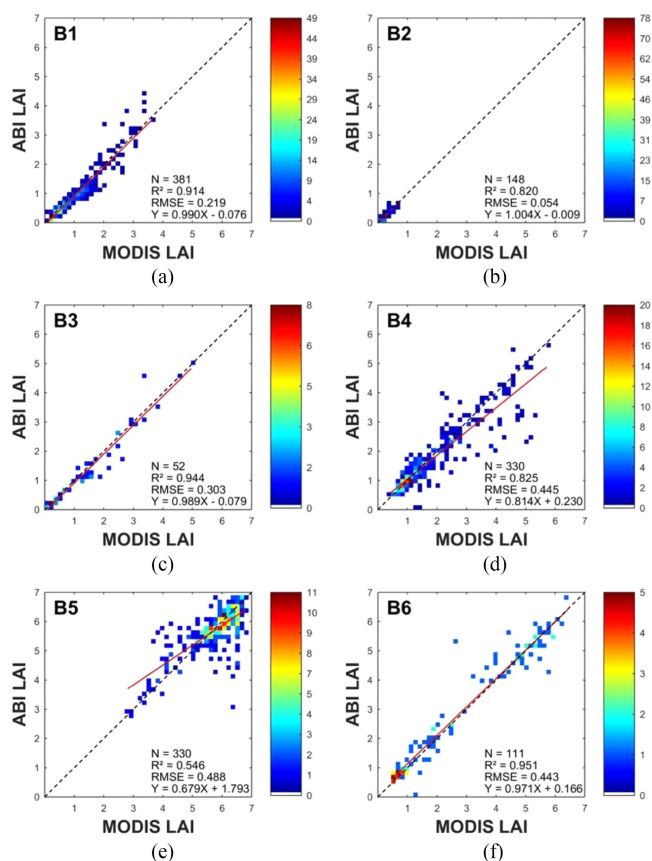


Fig. 11. Density scatter plots for biome-specific comparison between ABI and MODIS LAI at the site scale from January to September of year 2018. (a) Grasses and cereal crops (B1). (b) Shrubs (B2). (c) Broadleaf crops (B3). (d) Savannas (B4). (e) Evergreen broadleaf forests (B5). (f) Deciduous broadleaf forests (B6). The dash black line represents the 1:1 line. The solid red line is the linear fit.

eight-day intervals from January to September of year 2018 over the sites were utilized in this analysis. Fig. 11 shows the density scatter plots for biome-specific LAI comparisons between ABI and MODIS, while the comparisons of FPAR per biome are

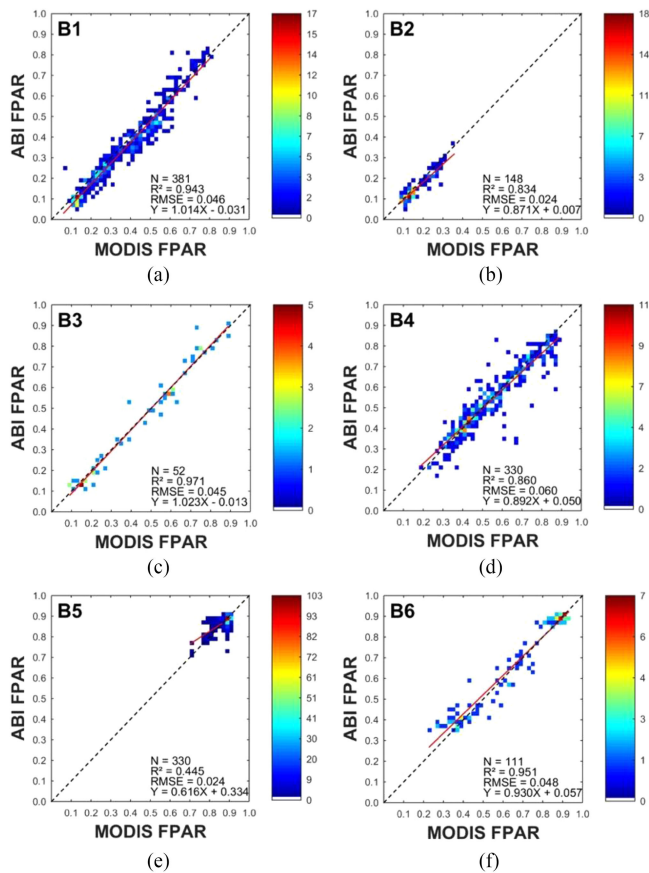


Fig. 12. Density scatter plots for biome-specific comparison between ABI and MODIS FPAR at the site scale from January to September of year 2018. (a) Grasses and cereal crops (B1). (b) Shrubs (B2). (c) Broadleaf crops (B3). (d) Savannahs (B4). (e) Evergreen broadleaf forests (B5). (f) Deciduous broadleaf forests (B6). The dash black line represents the 1:1 line. The solid red line is the linear fit.

depicted in Fig. 12. The statistical results of R^2 , RMSE, and regression equations are also provided. ABI retrievals match with MODIS products with overall R^2 values of 0.961 for LAI and 0.970 for FPAR, and RMSE values of 0.434 for LAI and 0.049 for FPAR. Except for Biome 5, R^2 for most biomes is larger than 80%, indicating that ABI retrievals from most biomes are able to capture greater than 80% of variation in MODIS products. Most biomes, except Biome 5, show consistency between ABI and MODIS LAI/FPAR, as the density scatters mostly distributes closely along the 1:1 line. Less agreement is observed in the case of dense evergreen broadleaf forest for both LAI (R^2 of 0.546 and RMSE of 0.488) and FPAR (R^2 of 0.445 and RMSE of 0.024). Unsurprisingly, this is mainly because of reflectance saturation for dense forests. The difference of compositing and off-nadir view zenith angle of ABI are possible the minor factors that result in the inconsistency between ABI and MODIS retrievals [29].

D. Direct Validation With Ground Measurements

The accuracy assessment was analyzed over the benchmark GBOV dataset. Fig. 13 presents the scatter-plots between ABI LAI/FPAR retrievals and the synthesized ground data from

GBOV. The relevant statistics are also summarized and provided in Fig. 13. The direct comparison of the ground-based high-resolution maps and the ABI products was performed at $3 \text{ km} \times 3 \text{ km}$ spatial resolution that allows limiting the effects of point spread function and geometric accuracy [10].

Good correlation between ABI products and ground data was observed for both LAI and FPAR, with R^2 of 0.81 for LAI and 0.85 for FPAR. Both LAI and FPAR show underestimation tendency with a negative bias of -0.40 for LAI and a negative bias of -0.03 for FPAR. The ABI FPAR displays an overall uncertainty with RMSE of 0.12 and relative RMSE of 19.3%, while LAI shows a larger uncertainty with RMSE of 0.95 and relative RMSE of 34.7%. This is mainly because the large LAI discrepancy in the case of saturation in dense forest. The percentage of FPAR pixels meets the target GCOS accuracy requirements is 61.98% for LAI and 41.32% for FPAR. Both LAI and FPAR cannot totally satisfy the GCOS requirements [max (0.5, 20%) for LAI and max (0.05, 10%) for FPAR]. We should note that the uncertainty of LAI/FPAR products could come from other sources, such as the uncertainty of ground measurements and spatial and temporal mismatch, although we have taken efforts to reduce the uncertainties brought by such factors. Additionally, only 20 sites and 3 biome types are included, which are spatiotemporally limited and not sufficient to qualify the accuracy of ABI LAI/FPAR retrievals. In summary, the comparisons reveal a good fit between ABI LAI/FPAR retrievals and ground measurements from GBOV, as well as acceptable uncertainties of ABI products. Large disagreement between ABI and ground measured LAI is observed in high LAI domains, which is consistent with the results in Section III-C.

V. DISCUSSION

A number of LAI/FPAR products have been generated from varying satellite observations [6]–[10]. The spatial and temporal gaps caused by contamination of cloud and aerosol limit the application of the products, especially for the LEO sensors (i.e., MODIS and VIIRS). Another non-negligible issue is that the spatiotemporal inconsistency between the different versions of LAI/FPAR products. In this article, we proposed a method of transplanting MODIS LAI/FPAR algorithm to GEO sensor ABI to retrieve LAI/FPAR. Figs. 7 and 8 demonstrate that using ABI observations can greatly increase the spatial and temporal continuity, benefiting from the hyper temporal resolution. The intercomparison with MODIS shows agreement between ABI and MODIS LAI/FPAR in terms of both spatial and temporal scales (Figs. 7–12). These results suggest that the GEO sensor outperforms LEO sensor in spatiotemporal completeness of LAI/FPAR products and the proposed approach of parametric optimization can adapt MODIS LAI/FPAR algorithm to other optical sensors, like ABI.

However, Figs. 7–12 also show the underestimations of ABI products when compared to MODIS LAI/FPAR, which mainly exist in dense forests. This is also revealed by the direct validation to ground measurements (see Fig. 13). MODIS products have shown underestimations particularly for deciduous and needle-leaf forests due to the reflectance saturation. Hence, taking the

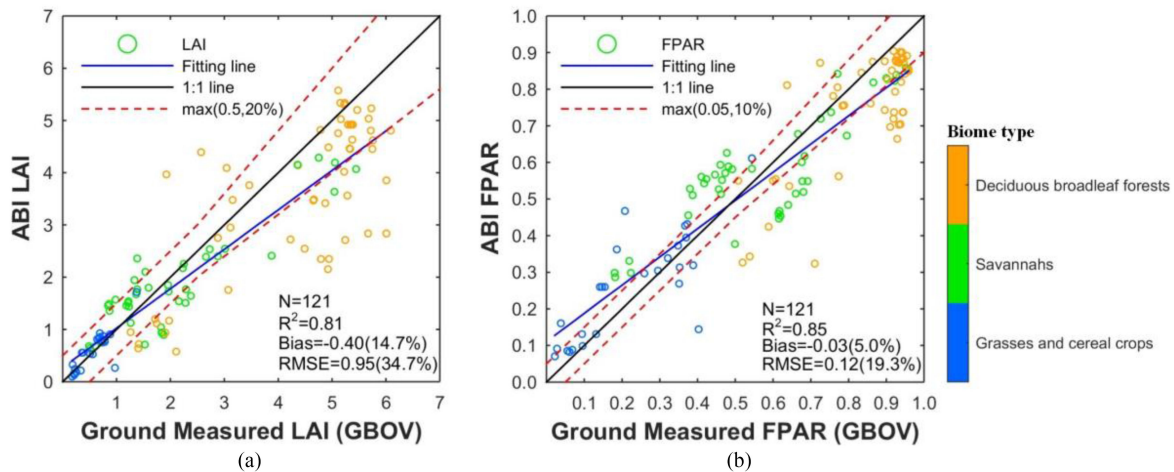


Fig. 13. Comparison between ground measurements and ABI products. (a) ABI LAI versus field measured LAI (GBOV). (b) ABI FPAR versus field measured FPAR (GBOV). The circles in each panel represent the satellite observations and ground measurements at the $3 \text{ km} \times 3 \text{ km}$ sites, and the different colors used to depict the circles represent the dominated biome types. The solid black line represents a 1:1 relationship. The dash red lines show the target GCOS specifications boundaries [max (0.5, 20%) for LAI and max (0.05, 10%) for FPAR]. The relevant statistics are also summarized, such as R², bias (relative bias is shown in brackets) and RMSE (relative RMSE is shown in brackets).

MODIS LAI as reference to adapt MODIS algorithm to ABI brings a risk that the problem of MODIS algorithm and products will also be transplanted to ABI. More efforts should be made in improvement of 3-D RT LAI/FPAR algorithm and generation of high-accuracy LAI reference.

The cross-comparison with MODIS products were conducted on representative examples and limited time series. The insufficient and inhomogeneous distribution also affected the validation with ground data. Further validation efforts are still necessary to ensure the product quality, as well as the exploration of possibility or potential of the ABI LAI/FPAR product with higher temporal frequency.

The successful transplanting of LAI/FPAR algorithm between LEO and GEO sensors and the consistency of different LAI/FPAR products imbue confidence in combining multiple sensors to retrieve improved LAI/FPAR products. Therefore, an implication of this article is the possibility of generating long-term LAI/FPAR records with higher temporal resolution and less spatiotemporal gaps based on multiple sensors observations.

VI. CONCLUSION

The latest GEO satellite GOES-16 is equipped with sensors able to measure reflectance at comparable spatial and spectral resolutions as LEO satellites like MODIS and VIIRS, but with the advantage of unprecedented high frequency. The subhourly image capturing capability of GOES-16 ABI greatly increases probability of cloud-free and more frequent LAI/FPAR products and expands upon LEO-based land applications, such as capturing phenology and monitoring landscapes in a timely manner. However, the operational LAI/FPAR algorithm for LEO satellites like MODIS cannot be directly applied for GOES-16 ABI, due to the discrepancy between sensors. Thus, the strategies for parametric optimization were proposed to prototype MODIS-comparable LAI/FPAR retrievals from GOES-16 ABI data, supported by the RT theory of canopy spectral invariants.

The configurable parameters were adjusted by SCE-UA optimization algorithm until the solution with minimum difference between ABI and MODIS products and maximum algorithm execution was located. After ABI-specific parameterization was successfully completed, ABI LAI/FPAR products were generated using the newly optimized ABI-LUT and comprehensive evaluation of the retrievals were conducted.

Our results indicate that the efforts of sensor-specific parameter optimization can successfully reduce the inconsistency of LAI/FPAR products between ABI and MODIS and increase the main algorithm execution rate, which will contribute to quality improvement of retrievals. The comparisons between the MODIS and ABI retrievals at different scales indicate strong agreement and spatiotemporal consistency between them. Acceptable uncertainty was proved by comparison to upscale products using high quality in-situ measurements. Moreover, the approach of parametric optimization by SCE-UA is applicable to any optical sensors for LAI/FPAR derivation; especially benefit other GEOS sensors, i.e., Himawari-8, FengYun-4A, Geo-KOMPSAT 2A, etc.

ACKNOWLEDGMENT

The authors would like to thank the NASA Ames Research Center for providing the GOES-16 ABI BRF data.

REFERENCES

- [1] J. M. Chen and T. A. Black, "Defining leaf area index for non-flat leaves," *Plant, Cell Environ.*, vol. 15, no. 4, pp. 421–429, 1992.
- [2] R. B. Myneni and D. L. Williams, "On the relationship between FAPAR and NDVI," *Remote Sens. Environ.*, vol. 49, no. 3, pp. 200–211, 1994.
- [3] M. R. Ramezani, A. R. M. Bavani, M. Jafari, A. Binesh, and S. Peters, "Investigating the leaf area index changes in response to climate change (case study: Kasilian catchment, Iran)," *SN Appl. Sci.*, vol. 2, no. 3, pp. 1–11, 2020.
- [4] J. Richetti, K. J. Boote, G. Hoogenboom, J. Judge, J. A. Johann, and M. A. Uribe-Opazo, "Remotely sensed vegetation index and LAI for parameter determination of the CSM-CROPGRO-Soybean model when in situ data are not available," *Int. J. Appl. Earth Observ.*, vol. 79, pp. 110–115, 2019.

- [5] Y. Song, J. Wang, Q. Yu, and J. Huang, "Using MODIS LAI data to monitor spatio-temporal changes of winter wheat phenology in response to climate warming," *Remote Sens.*, vol. 12, no. 5, pp. 786, 2020.
- [6] R. B. Myneni *et al.*, "Global products of vegetation leaf area and fraction absorbed PAR from year one of MODIS data," *Remote Sens. Environ.*, vol. 83, no. 1-2, pp. 214–231, 2002.
- [7] K. Yan *et al.*, "Generating global products of LAI and FPAR from SNPP-VIIRS data: Theoretical background and implementation," *IEEE Trans. Geosci. Remote Sens.*, vol. 56, no. 4, pp. 2119–2137, Apr. 2018.
- [8] Z. Zhu *et al.*, "Global data sets of vegetation leaf area index (LAI)3g and fraction of photosynthetically active radiation (FPAR) 3g derived from global inventory modeling and mapping studies (GIMMS) normalized difference vegetation index (NDVI3g) for the period 1981 to 2011," *Remote Sens.*, vol. 5, no. 2, pp. 927–948, 2013.
- [9] Z. Xiao *et al.*, "Use of general regression neural networks for generating the GLASS leaf area index product from time-series MODIS surface reflectance," *IEEE Trans. Geosci. Remote Sens.*, vol. 52, no. 1, pp. 209–223, Jan. 2014.
- [10] F. Baret *et al.*, "GEOV1: LAI and FAPAR essential climate variables and FCOVER global time series capitalizing over existing products. Part I: Principles of development and production," *Remote Sens. Environ.*, vol. 137, pp. 299–309, 2013.
- [11] C. Chen *et al.*, "China and India lead in greening of the world through land-use management," *Nat. Sustain.*, vol. 2, no. 2, pp. 122–129, 2019.
- [12] P. C. Saksa, R. C. Bales, C. L. Tague, J. J. Battles, B. W. Tobin, and M. H. Conklin, "Fuels treatment and wildfire effects on runoff from sierra nevada mixed-conifer forests," *Ecohydrology*, vol. 13, no. 3, 2020, Art. no. e2151.
- [13] Z. Shao, Y. Pan, C. Diao, and J. Cai, "Cloud detection in remote sensing images based on multiscale features-convolutional neural network," *IEEE Trans. Geosci. Remote Sens.*, vol. 57, no. 6, pp. 4062–4076, Jun. 2019.
- [14] P. Zhang *et al.*, "General comparison of FY-4A/AGRI with other GEO/LEO instruments and its potential and challenges on non-meteorological applications," *Front. Earth Sci.*, vol. 6, Dec. 2018, Art. no. 224.
- [15] K. Bessho *et al.*, "An introduction to himawari-8/9—Japan's new-generation geostationary meteorological satellites," *J. Meteorol. Soc. Jpn. Ser. II*, vol. 94, no. 2, pp. 151–183, 2016.
- [16] S. Hong, D.-B. Shin, B. Park, and D. So, "Development of prototype algorithms for quantitative precipitation nowcasts from AMI onboard the GEO-KOMPSAT-2A satellite," *IEEE Trans. Geosci. Remote Sens.*, vol. 54, no. 12, pp. 7149–7156, Dec. 2016.
- [17] J. McCorkel, B. Efremova, J. Hair, M. Andrade, and B. Holben, "GOES-16 ABI solar reflective channel validation for earth science application," *Remote Sens. Environ.*, vol. 237, 2020, Art. no. 111438.
- [18] R. Fensholt, A. Anyamba, S. Stisen, I. Sandholt, E. Pak, and J. Small, "Comparisons of compositing period length for vegetation index data from polar-orbiting and geostationary satellites for the cloud-prone region of West Africa," *Photogramm. Eng. Remote Sens.*, vol. 73, no. 3, pp. 297–309, 2007.
- [19] D. Yan, X. Zhang, Y. Yu, and W. Guo, "A comparison of tropical rainforest phenology retrieved from geostationary (SEVIRI) and polar-orbiting (MODIS) sensors across the Congo basin," *IEEE Trans. Geosci. Remote Sens.*, vol. 54, no. 8, pp. 4867–4881, Aug. 2016.
- [20] K. Guan, D. Medvigy, E. F. Wood, K. K. Caylor, S. Li, and S.-J. Jeong, "Deriving vegetation phenological time and trajectory information over Africa using SEVIRI daily LAI," *IEEE Trans. Geosci. Remote Sens.*, vol. 52, no. 2, pp. 1113–1130, Feb. 2014.
- [21] T. J. Schmit, P. Griffith, M. M. Gunshor, J. M. Daniels, S. J. Goodman, and W. J. Lebar, "A closer look at the ABI on the GOES-R series," *Bull. Amer. Meteorol. Soc.*, vol. 98, no. 4, pp. 681–698, 2017.
- [22] K. Yan *et al.*, "Evaluation of MODIS LAI/FPAR product collection 6. Part 1: Consistency and improvements," *Remote Sens.*, vol. 8, no. 5, pp. 359, 2016.
- [23] K. Yan *et al.*, "Evaluation of MODIS LAI/FPAR product collection 6. Part 2: Validation and intercomparison," *Remote Sens.*, vol. 8, no. 6, pp. 460, 2016.
- [24] H. Jin *et al.*, "Intercomparison and validation of MODIS and GLASS leaf area index (LAI) products over mountain areas: A case study in southwestern china," *Int. J. Appl. Earth Obs.*, vol. 55, pp. 52–67, 2017.
- [25] Y. Chen *et al.*, "Generation and evaluation of LAI and FPAR products from himawari-8 advanced himawari imager (AHI) data," *Remote Sens.*, vol. 11, no. 13, 2019, Art. no. 1517.
- [26] Y. Wang, G. Yan, R. Hu, D. Xie, and W. Chen, "A scaling-based method for the rapid retrieval of FPAR from fine-resolution satellite data in the remote-sensing trend-surface framework," *IEEE Trans. Geosci. Remote Sens.*, vol. 58, no. 10, pp. 7035–7048, Oct. 2020.
- [27] W. Hou, J. Su, W. Xu, and X. Li, "Inversion of the fraction of absorbed photosynthetically active radiation (FPAR) from FY-3C MERSI data," *Remote Sens.*, vol. 12, no. 1, 2019.
- [28] S. Ganguly *et al.*, "Generating vegetation leaf area index earth system data record from multiple sensors. Part 1: Theory," *Remote Sens. Environ.*, vol. 112, no. 12, pp. 4333–4343, 2008.
- [29] B. Xu *et al.*, "Analysis of global LAI/FPAR products from VIIRS and MODIS sensors for spatio-temporal consistency and uncertainty from 2012–2016," *Forests*, vol. 9, no. 2, 2018, Art. no. 73.
- [30] S. Ganguly *et al.*, "Generating vegetation leaf area index earth system data record from multiple sensors. Part 2: Implementation, analysis and validation," *Remote Sens. Environ.*, vol. 112, no. 12, pp. 4318–4332, 2008.
- [31] C. Chen *et al.*, "Prototyping of LAI and FPAR retrievals from MODIS multi-angle implementation of atmospheric correction (MAIAC) data," *Remote Sens.*, vol. 9, no. 4, pp. 370, 2017.
- [32] Q. Y. Duan, V. K. Gupta, and S. Sorooshian, "Shuffled complex evolution approach for effective and efficient global minimization," *J. Optim. Theory Appl.*, vol. 76, no. 3, pp. 501–521, 1993.
- [33] A. I. Lyapustin *et al.*, "Multi-angle implementation of atmospheric correction for MODIS (MAIAC): 3. Atmospheric correction," *Remote Sens. Environ.*, vol. 127, pp. 385–393, 2012.
- [34] A. Lyapustin and Y. Wang, "MCD19A1 MODIS/Terra+Aqua land surface BRF daily L2G global 500m and 1km SIN grid V006," *NASA EOSDIS Land Processes DAAC*, 2018. [Online]. Available: https://lpdaac.usgs.gov/documents/110/MCD19_User_Guide_V6.pdf
- [35] R. B. Myneni, Y. Knyazikhin, and T. Park, "MOD15A2H MODIS/Terra leaf area Index/FPAR 8-Day L4 global 500m SIN grid V006," *NASA EOSDIS Land Processes DAAC*, 2015. [Online]. Available: https://lpdaac.usgs.gov/documents/624/MOD15_User_Guide_V6.pdf
- [36] M. Friedl and D. Sulla-Menashe, "MCD12Q1 MODIS/Terra+Aqua land cover type yearly L3 global 500m SIN grid V006," *NASA EOSDIS Land Processes DAAC*, 2019. [Online]. Available: https://lpdaac.usgs.gov/documents/101/MCD12_User_Guide_V6.pdf
- [37] L. A. Brown *et al.*, "Evaluation of global leaf area index and fraction of absorbed photosynthetically active radiation products over North America using copernicus ground based observations for validation data," *Remote Sens. Environ.*, vol. 247, 2020, Art. no. 111935.
- [38] Y. Knyazikhin, "MODIS leaf area index (LAI) and fraction of photosynthetically active radiation absorbed by vegetation (FPAR) product (MOD 15) algorithm theoretical basis document," 1999. [Online]. Available: <http://eospsa.gsfc.nasa.gov/atbd/modistabls.html>
- [39] J. Pu *et al.*, "Evaluation of the MODIS LAI/FPAR algorithm based on 3D-RTM simulations: A case study of grassland," *Remote Sens.*, vol. 12, no. 20, 2020, Art. no. 3391.
- [40] K. Yan *et al.*, "Performance stability of the MODIS and VIIRS LAI algorithms inferred from analysis of long time series of products," *Remote Sens. Environ.*, vol. 260, 2021, Art. no. 112438.
- [41] Y. Knyazikhin, J. V. Martonchik, R. B. Myneni, D. J. Diner, and S. W. Running, "Synergistic algorithm for estimating vegetation canopy leaf area index and fraction of absorbed photosynthetically active radiation from MODIS and MISR data," *J. Geophys. Res. Atmos.*, vol. 103, no. D24, pp. 32257–32275, 1998.
- [42] T. Park, K. Yan, C. Chen, B. Xu, Y. Knyazikhin, and R. Myneni, "VIIRS leaf area index (LAI) and fraction of photosynthetically active radiation absorbed by vegetation (FPAR) product algorithm theoretical basis document (ATBD)," 2018. [Online]. Available: https://viirsland.gsfc.nasa.gov/PDF/VIIRS_LAI_FPAR_ATBD_V1.1.pdf
- [43] M. Mörtus and P. T. Stenberg, "A simple parameterization of canopy reflectance using photon recollision probability," *Remote Sens. Environ.*, vol. 112, no. 4, pp. 1545–1551, 2008.
- [44] Y. Wang *et al.*, "Investigation of product accuracy as a function of input and model uncertainties: Case study with SeaWiFS and MODIS LAI/FPAR algorithm," *Remote Sens. Environ.*, vol. 78, no. 3, pp. 299–313, 2001.
- [45] A. N. Tikhonov, A. Goncharsky, V. Stepanov, and A. G. Yagola, *Numerical Methods For the Solution of Ill-Posed Problems*. New York, NY, USA: Springer, 2013.
- [46] X. Song, C. Zhan, and J. Xia, "Integration of a statistical emulator approach with the SCE-UA method for parameter optimization of a hydrological model," *Chin. Sci. Bull.*, vol. 57, no. 26, pp. 3397–3403, 2012.
- [47] Y. Chen, K. Sun, D. Li, T. Bai, and C. Huang, "Radiometric cross-calibration of gf-4 pms sensor based on assimilation of landsat-8 oli images," *Remote Sens.*, vol. 9, no. 8, 2017, Art. no. 811.

- [48] M. R. Naeini, B. Analui, H. V. Gupta, Q. Duan, and S. Sorooshian, "Three decades of the shuffled complex evolution (SCE-UA) optimization algorithm: Review and applications," *Sci. Iran.*, vol. 26, no. 4, pp. 2015–2031, 2019.
- [49] J. S. Iiames, R. G. Congalton, T. E. Lewis, and A. N. Pilant, "Uncertainty analysis in the creation of a fine-resolution leaf area index (LAI) reference map for validation of moderate resolution LAI products," *Remote Sens.*, vol. 7, no. 2, pp. 1397–1421, 2015.
- [50] Y. He, Y. Bo, L. Chai, X. Liu, and A. Li, "Linking in situ LAI and fine resolution remote sensing data to map reference LAI over cropland and grassland using geostatistical regression method," *Int. J. Appl. Earth Obs.*, vol. 50, pp. 26–38, 2016.



Yeppei Chen received the B.S. degree in geographic information systems from Hubei University, Wuhan, China, in 2015, and Ph.D. degree in photogrammetry and remote sensing from Wuhan University, Wuhan, China, in 2021. She is currently working toward the Ph.D. degree in photogrammetry and remote sensing with the School of State Key Laboratory of Information Engineering in Surveying, Mapping and Remote Sensing, Wuhan University, Wuhan, China.

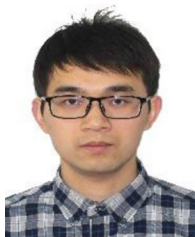
Her current research interests include radiometric calibration of sensor, LAI/FPAR inversion using re-

remote sensed data, and monitoring of vegetation dynamics.



Kaimin Sun received the B.S., M.S., and Ph.D. degrees in photogrammetry and remote sensing from Wuhan University, Wuhan, China, in 1999, 2004, and 2008, respectively.

He is currently a Professor with the State Key Laboratory of Information Engineering in Surveying, Mapping, and Remote Sensing, Wuhan University. His research interests include photogrammetry, object-oriented image analysis, and image change detection.



Wenzhuo Li received the B.S., M.S., and Ph.D. degrees in photogrammetry and remote sensing from Wuhan University, Wuhan, China, in 2011, 2013, and 2017, respectively.

He is currently a Postdoctoral Researcher with the State Key Laboratory of Information Engineering in Surveying, Mapping and Remote Sensing, Wuhan University. His current research interests include UAV positioning, UAV image processing and change detection, visual SLAM, land use and land cover changes detection, and object-oriented image analysis.



Chi Chen received the B.S. degree in remote sensing from Wuhan University, Wuhan, China, in 2013, and the M.A. and Ph.D. degrees in environmental remote sensing and geographical information system from Boston University, Boston, MA, USA, in 2015, and 2020, respectively.

He is currently a Postdoctoral Researcher with Lawrence Berkeley National Laboratory, Boston University. He is also affiliated with the Department of Environmental Science, Policy and Management, University of California, Berkeley, Berkeley, CA,

USA. His research interests include radiative transfer modeling in land remote sensing, vegetation dynamics, land-atmosphere models and interactions, earth system modeling, and climate change.



Pengfei Li was born in Anyang, Henan Province, China, in 1989. He received the B.S. degree in geographic information system from Huazhong Agricultural University, Wuhan, China, in 2012, the M.S. degree in cartography and geographic information system and the Ph.D. degree in photogrammetry and remote sensing from Wuhan University, Wuhan, China, in 2015 and 2018, respectively.

From 2019 to 2020, he was an Assistant Professor with the Information Engineering University, Zhengzhou, China. Since 2020, he has been an Assistant Professor with Hubei University of Technology. He was the author of two articles and two inventions. His research interests include UAV photogrammetry and applications of UAV remote sensing in urgent responses.



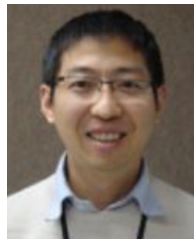
Ting Bai was born in 1992. She received the B.S. degree in geographic information systems from Huazhong Agricultural University, Wuhan, China, in 2014, and Ph.D. degree in photogrammetry and remote sensing from Wuhan University, Wuhan, China, in 2021. She currently working toward the five-years M.phil.-Ph.D. degree in photogrammetry and remote sensing from State Key Laboratory of Information Engineering in Surveying, Mapping and Remote Sensing, Wuhan University, Wuhan, China.

Her current research interests include remote sensing and feature fusion, machine learning, ensemble learning, deep learning, and land use and land cover change detection.



Taejin Park received the Ph.D. degree in geography with the Department of Earth and Environment, Boston University, Boston, MA, USA, in 2019.

He is currently a Postdoctoral Researcher with NASA Ames Research Center, Mountain View, CA, USA, and Bay Area Environmental Research Institute, Moffett Field, CA, USA. His research interests include the remote sensing of vegetation and climate-vegetation interactions.



Weile Wang received the B.S. and M.S. degrees in electrical engineering from Tsinghua University, Beijing, China, in 1997, and 2001, respectively, and the Ph.D. degree in physical geography from Boston University, Boston, MA, USA, in 2006.

He is currently a Research Scientist with NASA Ames Research Center, Mountain View, CA, USA and California State University Monterey Bay, CA, USA. His research interests include the Geostationary (GeoNEX) and hyperspectral (SBG) remote sensing, climate downscaling with statistical and dynamic models, global carbon cycle and climate interactions with stochastic models, terrestrial ecosystem modeling, and ecological forecasting with terrestrial observation and prediction system.



Ramakrishna R. Nemani received the M.S. degree in agricultural meteorology from Punjab Agricultural University, Ludhiana, India, in 1982, and the Ph.D. degree in forestry/remote sensing from the University of Montana, Missoula, MT, USA, in 1987.

He is currently a Research Scientist with NASA Ames Research Center, Moffett Field, CA, USA.



Ranga B. Myneni received the Ph.D. degree in biology from the University of Antwerp, Antwerp, Belgium, in 1985.

He is currently a Professor with Boston University, Boston, MA, USA. He is a Science Team Member of NASA MODIS and VIIRS projects. He has authored or coauthored more than 250 scientific articles in peer-refereed journals. His research interests include remote sensing of vegetation and climate-vegetation interactions.